nature geoscience

Supplementary information

https://doi.org/10.1038/s41561-026-02060-8

Limited remineralization of Arctic permafrost-derived organic carbon in nearshore marine sediments

In the format provided by the authors and unedited

The remineralization potential of permafrost organic carbon in nearshore marine sediments

Supplementary information

Sediment bulk parameters

TOC concentrations in YC22_MR_7 show little variation (Figure) throughout the core at an average of 1.10±0.05 wt% (*n*=24), with a single outlier of 0.93±0.4 wt% at the depth interval of 3-4 cm. Bulk $F^{14}C$ values ranged from 0.146±0.002 to 0.221±0.002, with an average of 0.1771±0.025 (*n*=12). This translates to apparent ^{14}C ages ranging from 12134±86 to 15619±88 ^{14}C years B.P., with an average of 13907±1126 ^{14}C yrs. $F^{14}C$ values of the lower part of the core (>13 cm) are considerably higher than above with 0.192±0.022 and 0.162±0.017, respectively. From the core top downwards, the TOC becomes slowly older, reaching its maximum age at 11 cm. Right below this depth, the TOC age is the youngest at 13 cm. Stable carbon isotope compositions are relatively constant throughout the core ranging from -27.1±0.3‰ to -28.0±0.1‰, with an average of -27.7±0.2‰, resembling bulk sedimentary isotopic values of local permafrost deposits[1]. Similar to the coastal site, TOC concentrations in YC22_MR_8 (basin site) were constant, however, slightly higher with 1.18±0.10 wt% (*n*=15). Bulk $F^{14}C$ and $\delta^{13}C$ values were on average higher in the basin than at the coastal site. $F^{14}C$ had an average of 0.205±0.020 (*n*=10), ranging from 0.187±0.001 to 0.244±0.001 and $\delta^{13}C$ was on average -25.9±0.3‰ (*n*=15), ranging from -25.4±0.1‰ to -26.5±0.1‰.

Biomarker analysis

Biomarker indices in YC22_MR_7 indicate a relatively homogeneous distribution throughout the core (Figure). The CPI of *n*-alkanes is at an average of 5.73±0.44 (*n*=27) with two minor excursions

to 4.45 at 3.5 cm and 4.44 at 22.5 cm, indicating a low maturity of the sedimentary OC[2]. GDGT-derived values of the BIT-Index are even more uniform, ranging from 0.72 to 0.76 with an average of 0.74±0.02 (*n*=27), indicating the sedimentary OC pool to be predominantly supplied by terrestrial OC[3]. Similarly uniform are hopanoid *ƒßß*-indices ranging from 0.43 to 0.46 with an average of 0.44±0.01 (*n*=25), pointing towards a constant contribution of petrogenic OC in the sediments[4]. Dinosterol contents were continuously low with an average of 1.6 ± 0.4 ng/g (*n*=22), indicating that marine primary production only contributes a minor fraction to the sedimentary OC pool[5]. Overall, the biomarker analysis indicates a strong dominance of terrestrial OC supply to the sediments, which is similarly reflected in bulk carbon isotopes. Biomarker parameters match well reported values of Grotheer et al. (2020)[6], who analyzed a core adjacent to our basin site. Organic matter degradability of the different sources in the sediments is strongly dependent on the nature of the organic matter, e.g. its molecular composition and whether it is present as dissolved or particulate, and mineral-bound vs. un-bound[7,8].

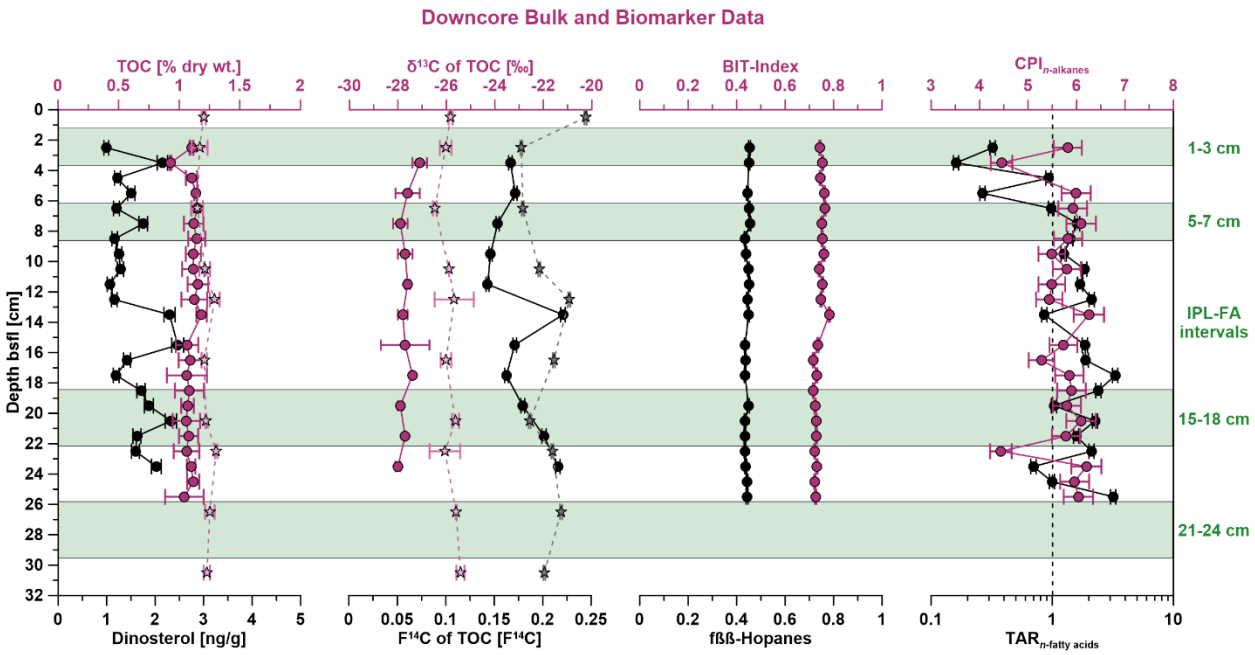

Figure S1: Downcore Bulk and Biomarker Data. Bulk and biomarker data of the coastal core site YC22_MR_7 (magenta and black dots) and basin site YC22_MR_8 (pink and gray stars). All data are displayed as mean values ± SD – Total organic carbon (TOC), stabile carbon isotopy ($\delta^{13}C$), radio carbon signature ($F^{14}C$), Dinosterol concentration, and fßß-Hopane concentrations uncertainties represent measurement uncertainties – calculated indices of the branched vs. isoprenoid tetraether index (BIT), carbon preference index (CPI), and terrestrial vs aquatic ratio (TAR) display propagated uncertainties of the individual measurements.

Porewater data of YC22_MR_7

Cl^- concentrations in the bottom water were 407±2 mmol/L (Figure). Throughout the sediment core, the Cl^- concentrations were fairly stable at 418±15 mmol/L (*n*=10) with one negative excursion at 13 cm at 380±1 mmol/L. SO_4^{2-} concentration changes follow the Cl^- pattern closely until 19 cm at an average of 20.8±1.1 mmol/L, including the negative excursion at 13 cm with 18.9±0.1 mmol/L. Thereafter, the SO_4^{2-} pattern diverges negatively from the Cl^- pattern.

Concentrations of both PO_4^{3-} and NH_4^+ are below the detection limit in the bottom water (Figure). Within the sediment, PO_4^{3-} concentrations remain below the detection limit until 7 cm, thereafter steadily increasing to 33.0±1.2 µmol/L at 19 cm, where concentrations plateau until the bottom of the core at 32.9±0.4 µmol/L.

Nitrate concentrations increase slightly from the water column concentration of 0.37±0.01 µmol/L to 0.53±0.08 µmol/L at 1 cm sediment depth and decrease thereafter to 0.13±0.03 µmol/L at 7 cm (Figure). Below 10 cm concentrations they are below the detection limit.

Calcium concentrations in the porewaters are elevated up to 25 cm, with an average of 354.8±11.7 mg/L (n = 8), in comparison to the bottom water concentrations of 331.3±0.6 mg/L. Concentrations are fairly stable, but display a maximum at 4 cm with 383.7±0.7 mg/L. At a depth of 28 cm, the concentrations exhibited a notable decline, reaching 298.0±0.2 mg/L.

Both dissolved iron and manganese are below the detection limit in the bottom water and at 1 cm sediment depth (Figure). Manganese concentrations increase rapidly to 2.18±0.01 mg/L at 4 cm and stay stable below at an average of 1.75±0.20 µmol/L (*n*=8). Iron concentrations increase more steadily than manganese concentrations to a maximum of 37.97±0.05 mg/L at 22 cm, with a slight decrease thereafter to 35.66±0.11 mg/L at 28 cm.

The porewater profiles of core YC22_MR_7 show redox-driven patterns typical of early diagenetic organic matter remineralization in sediments. Concentrations of NH_4^+, PO_4^{3-}, and Fe^{2+} increase with depth, while SO_4^{2-}, pH, and $\delta^{13}C$ of DIC decrease. These opposing trends reflect progressive microbial degradation of organic matter under diminishing electron acceptor availability[9]. NH_4^+ and PO_4^{3-} accumulation indicate the remineralization from nitrogen and phosphorus bearing organic substrates, whereas rising Mn^{2+} (4 cm) and Fe^{2+} (10 cm) concentrations point to reductive dissolution Mn/Fe-(hydr-)oxides as terminal electron acceptors become depleted[10]. Simultaneously decreasing SO_4^{2-} concentrations indicate sulfate-reducing conditions, characteristic of suboxic–anoxic diagenesis[9]. The gradual decline of pH is typically associated with proton release during aerobic-respiration, but may be partially buffered by carbonate dissolution indicated by slight Ca^{2+} decrease (details below)[11].

For the Qikiqtaruk near shore sediments, this pattern reflects remineralization of a heterogeneous OM pool derived from both coastal erosion of permafrost and modern marine productivity (see biomarker analysis), consistent with isotopic and geochemical evidence from nearby Yukon shelf sediments[12]. The measured DIC flux (0.18 mmol m^{-2} d^{-1}) is comparable to other Arctic shelf systems[13].

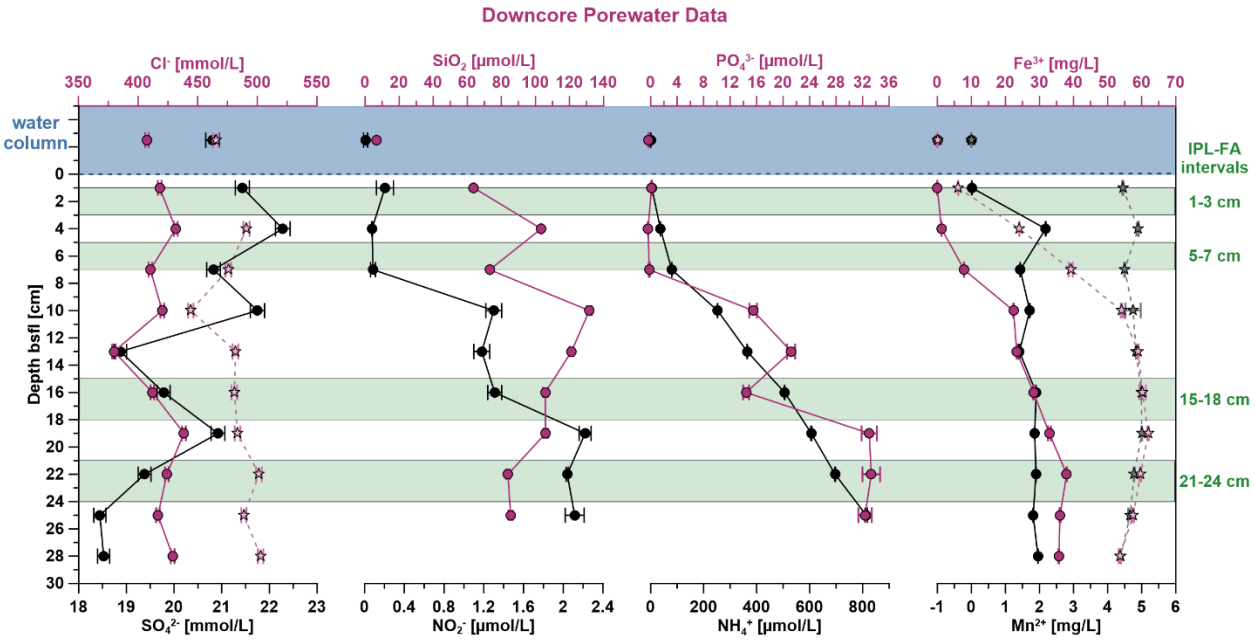

Figure S2: Downcore Porewater data. Porewater data of the coastal core site YC22_MR_7 (magenta and black dots) and basin site YC22_MR_8 (pink and gray stars). All data are displayed as mean values ± measurement uncertainties.

Intact Polar Lipid-Fatty Acid (IPL-FA) analysis

The quantification of intact polar lipids (IPL) of the polar lipid (PL) extract showed seven main contributing lipid classes in all four extracted sediment intervals. Within these, phosphate-bearing IPLs clearly dominated with diphosphatidyl glycerol (DPG), lyso-DPG, phosphatidyl ethanolamine (PE), phosphatidyl-(*N*)-methylethanolamine (PME), phosphatidyl choline (PC), and

phosphatidyl glycerol (PG) as main head group classes. In addition, minor contributions (<5%) of the aminolipid class of betaine lipids (BL) were detected in all four sediment intervals, declining in absolute concentrations from 66 to 30 ng/g. Relative abundance of DPG, lyso-DPG, and PME increased with increasing sediment depth by a factor of 2 to 3, while PG decreased from 40% to <1%. PE remained fairly constant throughout the core with ca. 9% and PC first exhibited a 4-fold decline below the surface layers, but increased in the bottom layer again. This shift in IPL composition from the surface to the deeper layers can be related to the change in bacterial community compositions as observed in the 16S rRNA analyses. While PG and PE are main lipids in many proteobacteria, including the Gammaproteobacteria, the increase of DPG and lyso DPG with depth is consistent with an increase of sulfate reducing bacteria as this is a dominant lipid in these organisms[14] and is also expected to increase due to energy limitation as cells in stationary phase tend to produce more DPG[15].

All phospholipid compounds dropped in absolute concentrations with depth with the exception of PME, which remained fairly constant between 60 to 90 ng/g, indicating a constant production of this IPL by benthic microorganisms. PME in organic-rich sediments has been previously assigned to heterotrophic activity[16]. While some of the detected IPLs could be derived from detrital algal sources in the surface, these include BL and PC[17], as their fatty acid composition in the surface layers also partly contain algal-specific PUFAs such as $C_{20:5}$ and $C_{22:6}$, for most compounds the fatty acid composition of predominantly C_{16}, C_{17}, and C_{15} fatty acids points to mainly benthic contribution to these lipids. Based on the relative abundance of the IPLs together with the dominant fatty acid compositions we identified the purified IPL-FA sources for isotope analysis to be mainly DPG and Lyso-DPG for $C_{15:0\text{-}br}$ FAME and PE, PME, PC, and PG for $C_{16:1}$ FAME.

The radiocarbon analysis on purified bacterial IPL-FAs of $C_{15\text{-}br}$ and $C_{16:1}$ revealed relatively uniform $F^{14}C$ values ranging from 0.806±0.013 to 0.931±0.016, with an average of 0.856±0.041 (*n*=8). $C_{15\text{-}br}$ displays slightly lower average $F^{14}C$ values in comparison to $C_{16:1}$ of 0.827±0.029 and 0.885±0.028, respectively. Similarly, stable carbon isotopic composition revealed a uniform distribution ranging from -23.3 to -25.1‰ with an average of -24.7±1.0‰ (*n*=7). However, $C_{16:1}$ in the 1-3 cm interval displayed much higher values of -19.0±1.3‰, likely due to input of algae detritus as indicated by higher betaine lipids abundance; therefore, this interval was excluded from subsequent estimates. Purified IPL-FAs isotope data were used to determine microbial substrate origins, using the same isotope end-member mixing model and end-members as for bulk sediments and DIC samples (see below). However, ^{13}C fractionation during fatty-acid biosynthesis, was estimated at -4 to -2‰[18] and accounted for before end-member modeling.

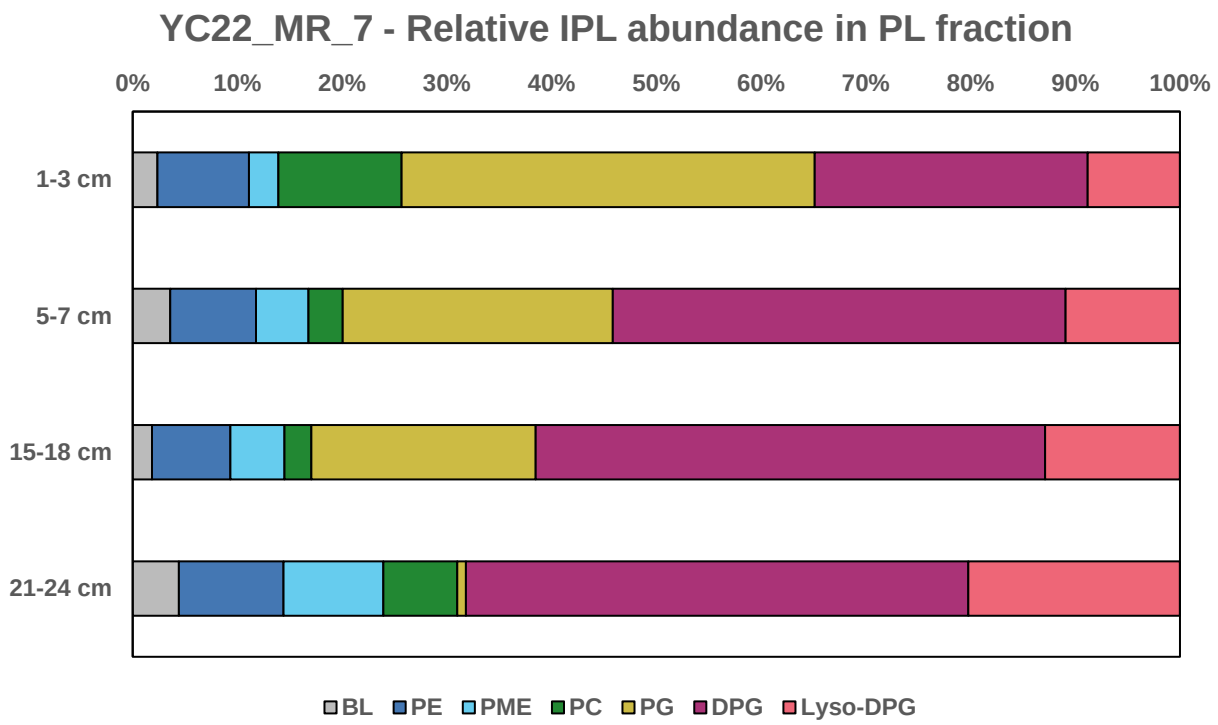

Figure S3: YC22_MR_7 Intact polar lipids. Abundances of intact polar lipids (IPL) in the extracted polar lipid (PL) fraction, representing the precursor lipids of the purification IPL-fatty acids used for compound-specific isotope analysis. Displayed IPLs are: betaine lipids (BL), phosphatidyl ethanolamine (PE), phosphatidyl-(N)-methylethanolamine (PME), phosphatidyl choline (PC), and phosphatidyl glycerol (PG), diphosphatidyl glycerol (DPG), and lyso-DPG (n=1 for each sample depth).

Mixing model and end-member values

The fractional contributions of OC from the Holocene permafrost including active layer and recent plant littler (OC_H), permafrost deposits (OC_P), and marine primary production (OC_M) were assessed by the following equations:

$$OC_H * F^{14}C_H + OC_P * F^{14}C_P + OC_M * F^{14}C_M = F^{14}C_{OC\ bulk} \qquad (1)$$

$$OC_H * \delta^{13}C_H + OC_P\delta^{13}C_P + OC_M\delta^{13}C_M = \delta^{13}C_{OC\ bulk} \quad (2)$$

$$OC_H + OC_P + OC_M = 1 \quad (3)$$

A previous study on permafrost coastal erosion along the Beaufort Sea coast has provided valuable insights into terrestrial end-member values[1]. It involved the collection of permafrost cores spanning from the tundra surface to below sea level in three dominant geomorphic terrain units near the Beaufort Sea coast. These units include i) the active layer which remained unaltered by thermokarst lake formation and drainage, ii) ancient and iii) young drained thermokarst lake basins. Downcore patterns reveal distinctions between the upper and lower sections of the cores (Bristol et al., 2021; Figure). The upper deposits, comprising the active layer and upper permafrost as well as lacustrine sediments formed during the Holocene, exhibit exceptionally high organic carbon (OC) content (12.1 wt.%), C/N ratio (18.3), and $F^{14}C$ (0.480±0.205) values but low $\delta^{13}C$ (−28.0±0.9‰) values. In contrast, the lower ice-rich old permafrost deposits feature low OC content (1.2 wt.%), C/N ratio (12), and $F^{14}C$ (0.007±0.005) values but high $\delta^{13}C$ (−26.0±0.8‰) values. These characteristics are indicative of Late Pleistocene permafrost deposits[1], and are also referred to as "Pleistocene Ice Complex Deposits"[19,20]. Therefore, $F^{14}C$ and $\delta^{13}C$ values for the Holocene permafrost including active layer (OC_H) are defined as 0.480±0.205 and −28.0±0.9‰, respectively, which includes the contribution of fresh terrestrial production. $F^{14}C$ and $\delta^{13}C$ values for Pleistocene permafrost deposits (OC_P) are defined as 0.007±0.005 and −26.0±0.8‰, respectively. $\delta^{13}C$ values for marine OC (OC_M) are defined as −21.0±2.6‰ based on measurements of marine phytoplankton[19], with ±2.6‰ uncertainty accounting for seasonal and annual changes in $\delta^{13}C_M$ over the last 50 years. Due to the lack of a ^{14}C time series of regional seawater dissolved inorganic carbon (DIC), a direct ^{14}C measurement

158 of DIC in the Beaufort Sea was used to define a $F^{14}C$ value (1.008±0.020) for marine OC in the
159 2010s[21]. $F^{14}C$ values of DIC before the 2000s are taken from a ^{14}C time series of cod otoliths in
160 the Barents Sea[22]. Note that while the $F^{14}C$ value of seawater DIC exhibits spatial differences in
161 the Arctic Ocean, these variations have minor effects on calculated results. Minor decay
162 corrections have been applied to all reported $F^{14}C$ values following the equation:

163 $$F^{14}C_y = F^{14}C * e^{(1950-y)/8267} \quad (4)$$

164 where y is the time of deposition [23], based on the sediment age model. Regarding $\delta^{13}C$ values of
165 bacterial PLFA, a ^{13}C fractionation ($\delta^{13}C_{biomass}$–$\delta^{13}C_{PLFA}$) factor of 2–4‰ is considered to derive the
166 $\delta^{13}C$ value of bulk biomass[24]. In addition, Arctic rivers produce substantial particulate OC through
167 primary production[25], however, the burial of OC from riverine primary production is negligible in
168 the coastal sediments due to its rapid degradation in river mouth[26].

169 End-member contributions were determined using Bayesian Markov chain Monte Carlo
170 simulations, applying arbitrary assignments of end-member values to minimize errors[27].
171 1,000,000 out of 100,000,000 random samples were taken from the normal distribution of each
172 end member within their mean and standard deviations to fulfill the given system in simulations.
173 The mean relative contributions and the standard deviation of different OC sources were then
174 estimated.

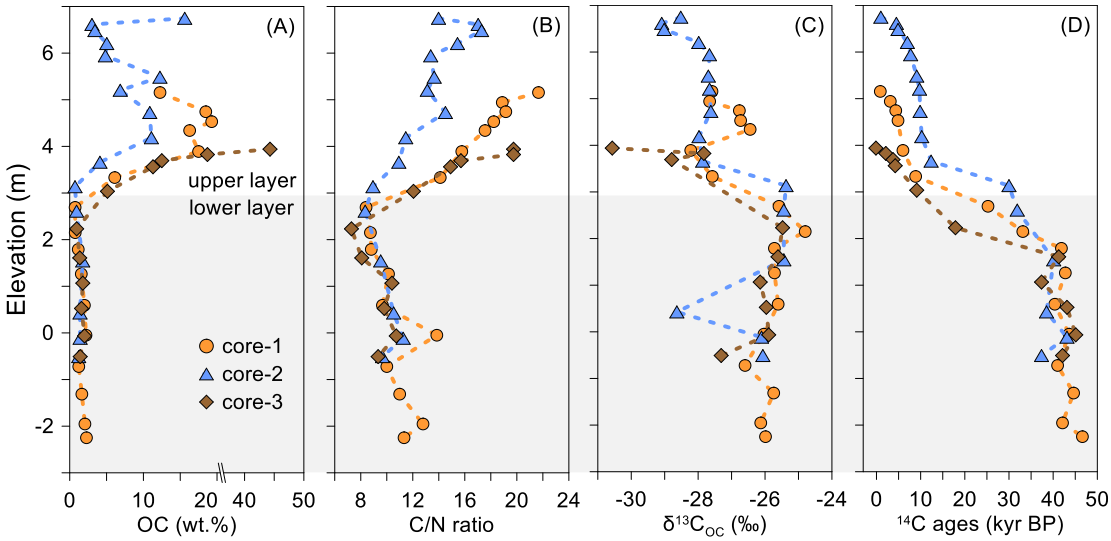

Figure S4: Holocene and Pleistocene endmembers. Profiles of (A) organic carbon (OC) content, (B) C/N ratio, (C) $\delta^{13}C$, and (D) $F^{14}C$ values of OC in three permafrost cores (data from Bristol et al. (2021)[1] representing reported mean values).

Holocene and Pleistocene endmembers from a dataset published by Bristol et al., (2021) because it derives from samples with reliable age constraints, which were obtained by coring directly into the permafrost body, clearly separating the Holocene and Pleistocene horizons. By contrast, samples taken at outcrops of the slumps or from mud debris involves the risk of including materials washed down from the overlying layers, which would carry a much younger radiocarbon age.

Herschel Island is a glacial push-moraine originating from an advance of the Laurentide Ice Sheet into the Northern Yukon during the Late Wisconsin (23 to 15 kyr BP)[28]. It is made up of redeposited marine and terrestrial sediments mixed into a glacial diamicton[29]. The sediments of Herschel Island exhibit widely variable OC ages, ranging from non-finite to modern[28]. However, previous findings of radiocarbon-free vertebrate samples (>50 ka)[30] strongly suggest that at least a subfraction of the organic carbon on Herschel Island is of comparable age as the older samples analyzed by Bristol et al., 2021.

While particulate organic carbon from the Mackenzie River and other streams are a likely additional source, this material itself is highly heterogeneous consisting of a mixture of Holocene, Pleistocene, petrogenic, and aquatic organic matter. An endmember should ideally be a homogenous material. We therefore did not consider river particulate OM a suitable endmember and argue that the fate of ancient terrestrial permafrost-derived carbon is best assessed by defining the broader Holocene and Pleistocene categories as primary endmembers. It has to be noted that any endmember analysis of such complex systems remains a quantitative approximation.

Age model constraints

The artificial radioisotope ^{137}Cs was detected throughout the 25 cm long core, except the top 3 cm, where it was below the detection limit. In the absence of intense mixing or vertical mobility, this indicates an age of the entire core younger than the year 1954, when global fallout is assumed to first have occurred [31]. The shape of the profile would indicate that the peak of ^{137}Cs in 1963 if present in this area, is below the sampling depth of the core.

There is a small, but clearly detectable fraction of ^{210}Pb in excess of its parent isotope ($^{210}Pb_{ex}$). This fraction shows a decrease throughout the core to almost nil but does not fully reach background levels, which prevents the application of a $^{210}Pb_{ex}$ constant rate of supply model (CRS). Therefore, tentative ages are constrained by the constant initial concentration (CIC)-approach and a constant flux, constant supply model (CFCS). Both models agree fairly well and indicate an age of 47.9 +- 7.6 years (CFCS) or 42 +- 28 years (CIC) respectively at a midpoint depth of 20.5 cm, which corresponds to the year 1975 (CFCS). The clear trend in the ^{210}Pb profile limits the extent of possible mixing that could affect the ^{137}Cs profile (Figure). ^{241}Am, another artificial radioisotope that is less prone to vertical relocation, was below the detection limit at all depths.

In summary, the radiometric constraints all point towards a sedimentation rate of around 0.50±0.07 cm year^{-1} and demonstrate that the sediment has been recently deposited.

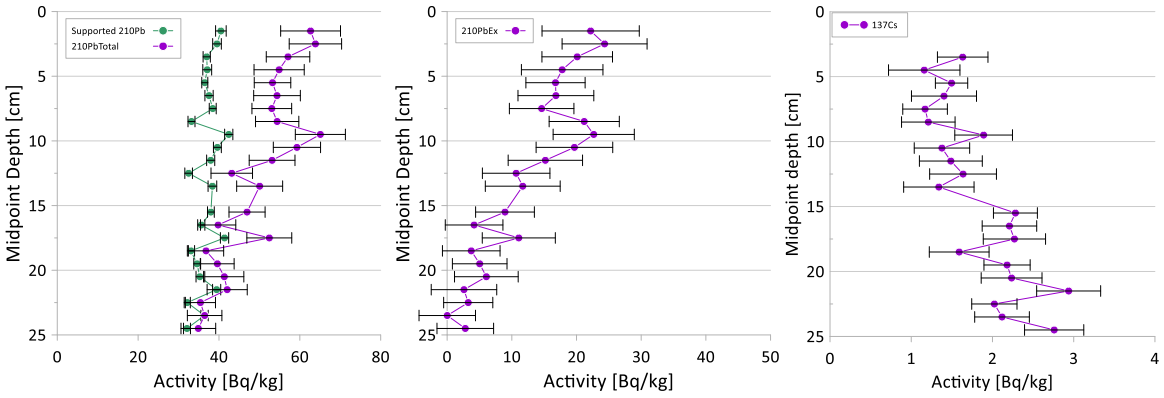

Figure S5: Age model data. Compilation of ^{210}Pb and ^{137}Cs data used for the sedimentary age model produced for sediment core YC22_MR_7. All values are shown with the analytical uncertainties from propagated counting errors (one standard deviation).

Benthic Microbial Community Composition

The microbial community composition was measured every 5 cm of the 25 cm long core at YC22_MR_7. The sample coverage was above 98.5% (Figure S6). Species richness ranged between 1220 and 1640 and peaked at 10 cm and 20 cm, while evenness appeared to increase towards 10 cm before decreasing again. The Shannon Diversity Index ranged from 106 to 638 and Inverse Simpson ranged from 20.9 to 252 (Figure S6). Accordingly, the beta-diversity showed a dominant contribution of Bacteroidia (e.g., *Flavobacterium* and *Lutibacter*), Gammaproteobacteria (e.g., *Woeseia*), and Verrucomicrobiae (e.g., *Rubritalea*) in the surface sediments (0-1 cm) (Figure S7). At 5 cm, a gradual shift from aerobic to anaerobic taxa with sediment depth is evident. Classes such as unclassified Desulfuromonadia were present in 5 and 10 cm, unclassified Desulfobacteria started being a dominant class in 10 cm, while

Desulfobacteria (e.g., *Desulfatiglans, SEEP-SRB1, Sva0081 Sediment Group*) became present at 15 cm depth (Figure S7). Additionally, unclassified Phycisphaerae (genus SG8-4) were also present in anoxic sediments (Figure S7).

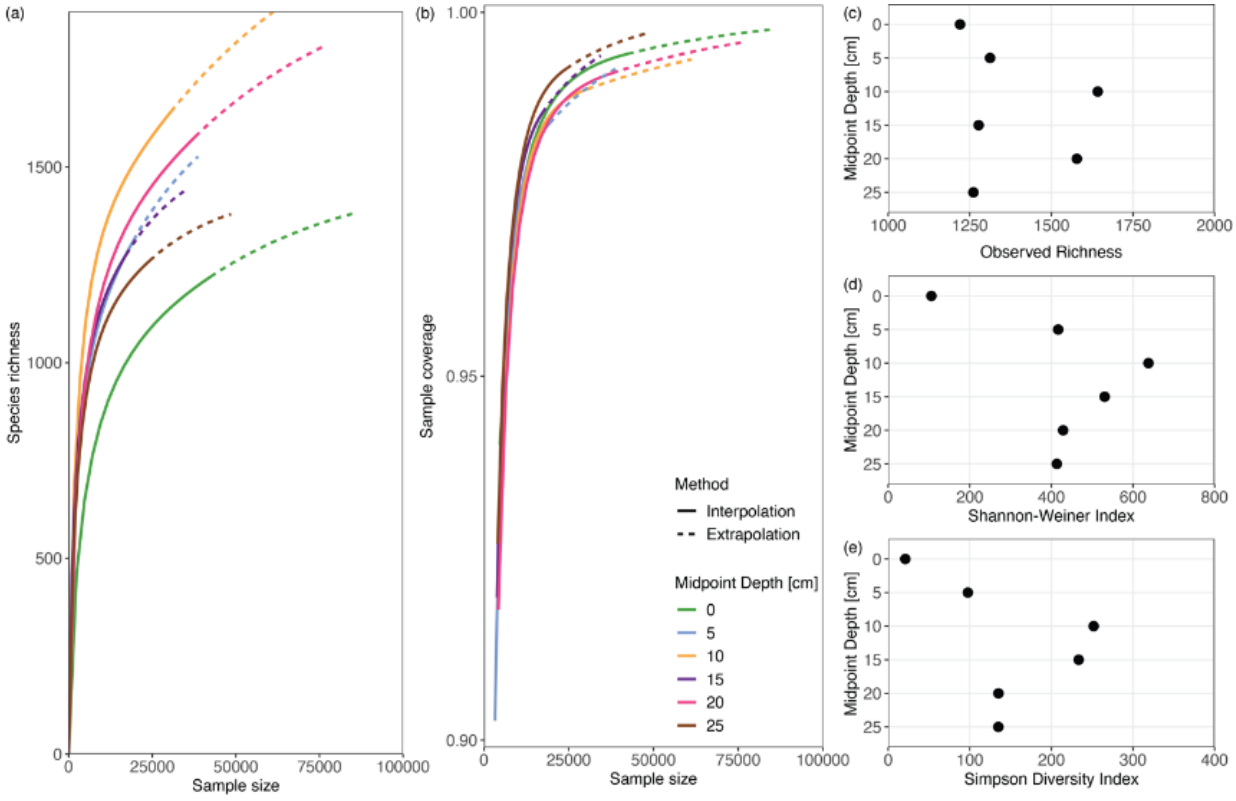

Figure S6: Alpha-diversity by depth. Rarefaction (a), coverage (b), Species richness (c), Shannon Diversity index (d), and Inverse Simpson index (e) – n=1 for each layer. Each colored line corresponds to an individual sample.

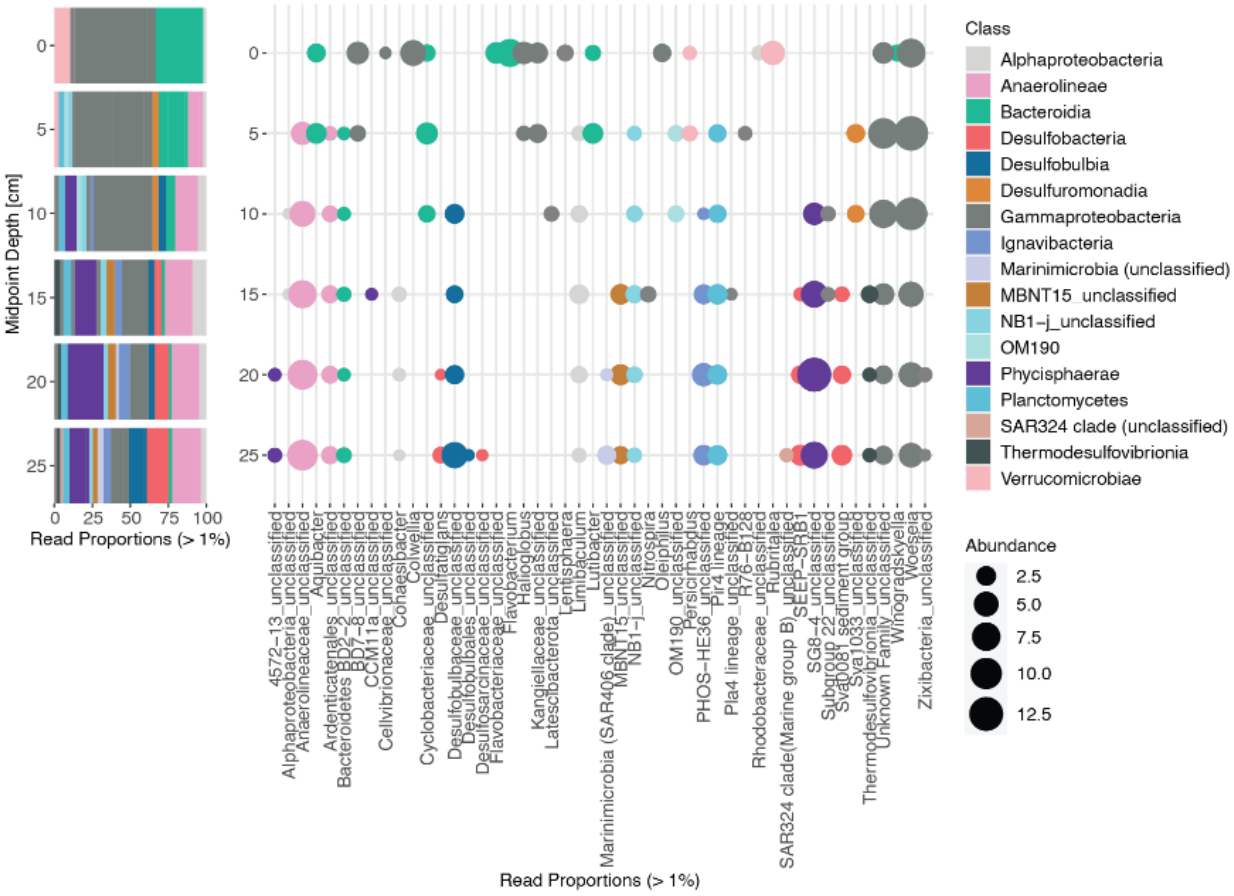

Figure S7: Microbial communities. Relative abundance of microbial community (n=1 for sample depth) on (left) class level and (right) genus level. The colors correspond to the class level and the increasing circle area represents a higher genus-level abundance. The cut-off is greater than 1% relative genus abundance.

Carbonate dissolution estimate

The R-package "AquaEnv"[32] estimates the acid-base chemistry and the carbonate equilibrium system, as well as the solubility products (Ksp) for aragonite and calcite. Using total DIC, ammonium, silicates, phosphates, nitrates, nitrites, sulfates and pH, as well as salinity, temperature and pressure, as input parameters, the R-function “aquaenv” estimates CO_3^{2-}, which can be used to calculate the saturation state (Ω) with respect to calcium carbonate with

$$\Omega = \frac{[Ca^{2+}][CO_3^{2-}]}{K_{sp}} \quad (5)$$

Based on the input parameters, it was determined that calcite is precipitating throughout the entire sediment depth, while aragonite is undergoing dissolution in most sediment depths (Figure S7). Core site YC22_MR_8 lacks pH data, preventing the determination of the DIC system. However, the DIC and Ca^{2+} concentrations are similar at both sites, suggesting that calcite and aragonite behavior may be analogous.

The dissolution of calcium carbonate yields equal amount of moles DIC[33]. Therefore, to estimate the contributions of DIC from aragonite dissolution, we compared the increase in Ca^{2+} to the DIC concentration in the porewaters at both sites relative to the concentrations in the bottom water. At the core site YC22_MR_7, the average calcium concentration was 348.5 mg/L, representing an increase of approximately 17.2 mg/L relative to the bottom water concentration (Figure S2), which is equivalent to 0.43 mmol/L. The average increase in DIC concentrations relative to the bottom water was 2.49 mmol/L. Core site YC22_MR_8, displaying analogous trends (Ca^{2+} data not shown), with Ca^{2+} increasing by approximately 0.75 mmol/L and DIC by 4.27 mmol/L relative to sea water. Thus, we estimate that approximately 17% of the DIC at both sites may be derived from aragonite dissolution. We therefore account for this fraction (including its isotopic signature) in our estimate for permafrost remineralization efficiency, using an isotope mass balance to exclude the 17% from aragonite dissolution from the initial DIC pool with its corresponding isotopic signature of $\delta^{13}C$=-5.2±1.2‰ and $F^{14}C$=0.014±0.064 (*n*=8) before applying the endmember model. Calculation was performed as followed for both $\delta^{13}C$ and $F^{14}C$:

$$\delta^{13}C_{calib} = \frac{\delta^{13}C_{original} * 100\% - (-5.2 \pm 1.2‰) * 17\%}{100\% - 17\%} \quad (6)$$

268 $$F^{14}C_{calib} = \frac{F^{14}C_{original} * 100\% - (0.014 \pm 0.064) * 17\%}{100\% - 17\%} \quad (7)$$

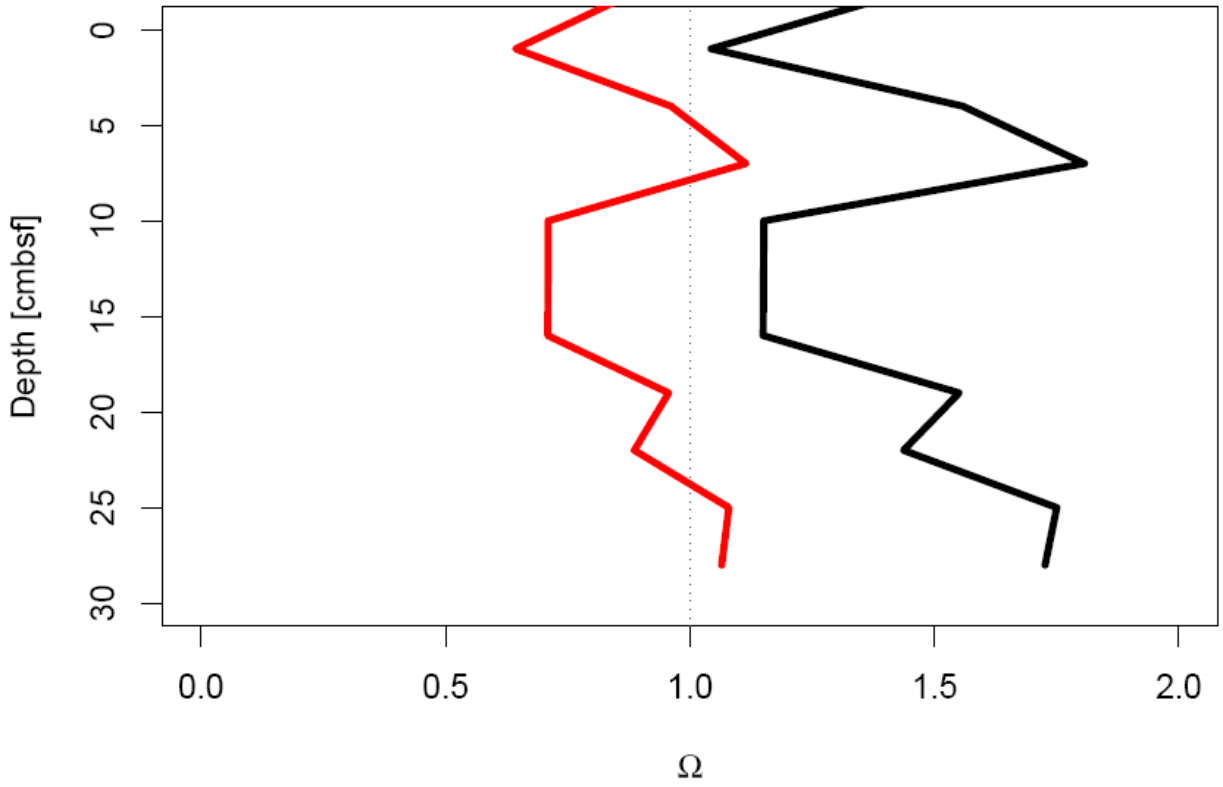

269

270 *Figure S8: Carbonate saturation state. Saturation state (Ω) of aragonite (red) and calcite (black)*

271 *in sediment core YC22_MR_7. Estimated Ω values above 1 indicate mineral precipitation, values*

272 *below 1 indicate mineral dissolution.*

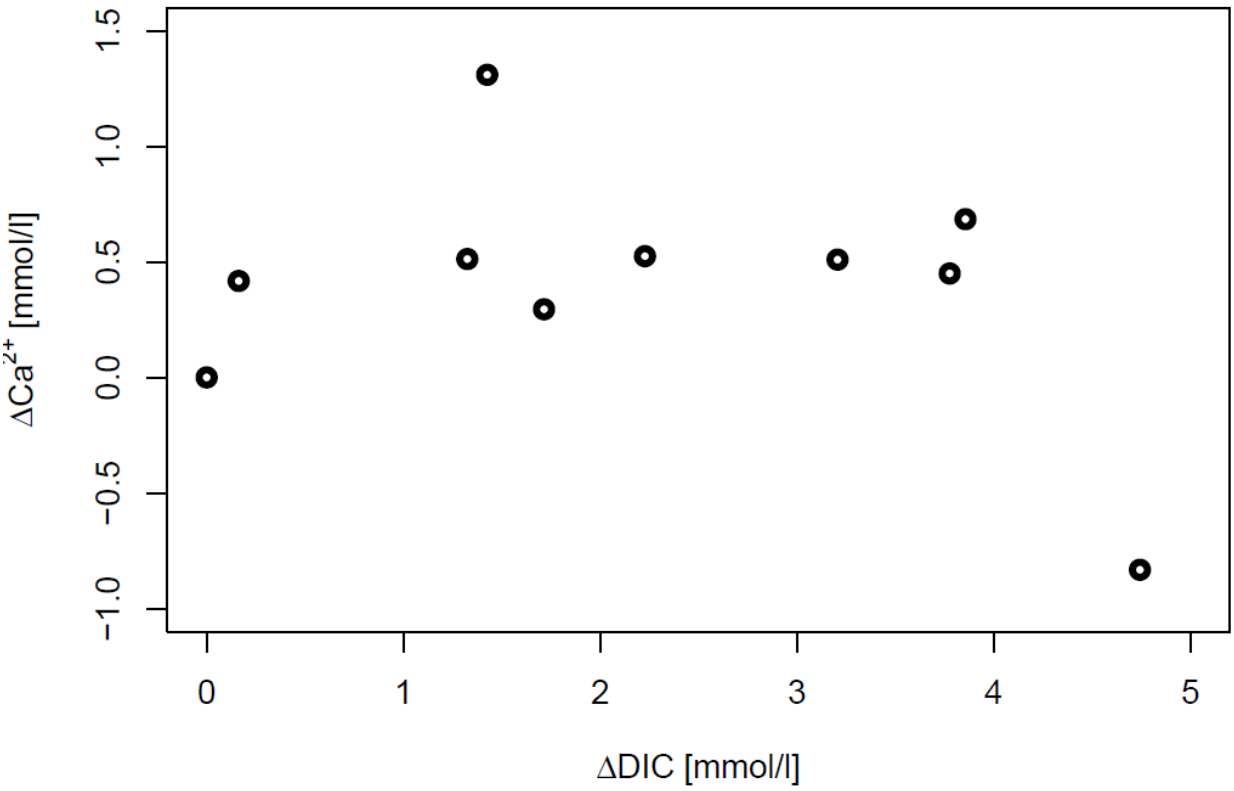

273

274 *Figure S9: Calcium - dissolved inorganic carbon. Concentration changes Ca^{2+} and dissolved*

275 *inorganic carbon (DIC) in porewaters of the coastal site YC22_MR_7, relative to seawater.*

276 *Represented data displays mean values of measurements.*

277

278 References

279 1. Bristol, E. M. *et al.* Geochemistry of coastal permafrost and erosion-driven organic
280 matter fluxes to the Beaufort Sea near Drew Point, Alaska. *Front. Earth Sci. (Lausanne).* **8**,
281 598933 (2021).

282 2. Bray, E. E. & Evans, E. D. Distribution of n-paraffins as a clue to recognition of source
283 beds. *Geochim. Cosmochim. Acta* **22**, 2–15 (1961).

284 3. Hopmans, E. C. *et al.* A novel proxy for terrestrial organic matter in sediments based on
285 branched and isoprenoid tetraether lipids. *Earth Planet. Sci. Lett.* **224**, 107–116 (2004).

4. Meyer, V. D. *et al.* Permafrost-carbon mobilization in Beringia caused by deglacial meltwater runoff, sea-level rise and warming. *Environmental Research Letters* **14**, 85003 (2019).

5. Fahl, K. & Stein, R. Biomarkers as organic-carbon-source and environmental indicators in the Late Quaternary Arctic Ocean: problems and perspectives. *Mar. Chem.* **63**, 293–309 (1999).

6. Grotheer, H. *et al.* Burial and Origin of Permafrost-Derived Carbon in the Nearshore Zone of the Southern Canadian Beaufort Sea. *Geophys. Res. Lett.* **47**, e2019GL085897 (2020).

7. Keskitalo, K. H. *et al.* Seasonal variability in particulate organic carbon degradation in the Kolyma River, Siberia. *Environmental Research Letters* **17**, 034007 (2022).

8. Shakil, S. *et al.* Low biodegradability of particulate organic carbon mobilized from thaw slumps on the Peel Plateau, NT, and possible chemosynthesis and sorption effects. *Biogeosciences* **19**, 1871–1890 (2022).

9. Jørgensen, B. B. *et al.* The biogeochemical sulfur cycle of marine sediments. *Front. Microbiol.* **10**, 849 (2019).

10. Burdige, D. J. Geochemistry of marine sediments. (2020).

11. Soetaert, K. *et al.* Reprint of "The effect of biogeochemical processes on pH". *Mar. Chem.* **106**, 380–401 (2007).

12. Radosavljevic, B. *et al.* Arctic Nearshore Sediment Dynamics—An Example from Herschel Island—Qikiqtaruk, Canada. *J. Mar. Sci. Eng.* **10**, 1589 (2022).

13. Bristol, E. M. *et al.* Geochemistry of coastal permafrost and erosion-driven organic matter fluxes to the Beaufort Sea near Drew Point, Alaska. *Front. Earth Sci. (Lausanne).* **8**, 598933 (2021).

14. Seidel, M. *et al.* Phosphate-free ornithine lipid contents in Desulfovibrio spp. respond to growth temperature. *Org. Geochem.* **59**, 133–142 (2013).

15. Hiraoka, S. *et al.* Active increase in cardiolipin synthesis in the stationary growth phase and its physiological significance in Escherichia coli. *FEBS Lett.* **336**, 221–224 (1993).

16. Schubotz, F. *et al.* Petroleum degradation and associated microbial signatures at the Chapopote asphalt volcano, Southern Gulf of Mexico. *Geochim. Cosmochim. Acta* **75**, 4377–4398 (2011).

17. Dembitsky, V. M. Betaine ether-linked glycerolipids: Chemistry and biology. *Prog. Lipid Res.* **35**, 1–51 (1996).

18. Hayes, J. M. Factionation of the Isotopes of Carbon and Hydrogen in Biosynthetic Processes. (2001).

19. Tesi, T. *et al.* Massive remobilization of permafrost carbon during post-glacial warming. *Nat. Commun.* **7**, 13653 (2016).

20. Martens, J. *et al.* Remobilization of dormant carbon from Siberian-Arctic permafrost during three past warming events. *Sci. Adv.* **6**, eabb6546 (2020).

21. Druffel, E. R. M. *et al.* Radiocarbon in dissolved organic and inorganic carbon of the Arctic Ocean. *Geophys. Res. Lett.* **44**, 2369–2376 (2017).

22. Kalish, J. M. *et al.* A time history of pre-and post-bomb radiocarbon in the Barents Sea derived from Arcto-Norwegian cod otoliths. *Radiocarbon* **43**, 843–855 (2001).

23. Reimer, P. J. *et al.* Discussion: reporting and calibration of post-bomb 14C data. *Radiocarbon* **46**, 1299–1304 (2004).

24. Hayes, J. M. Fractionation of the isotopes of carbon and hydrogen in biosynthetic processes, pp. 225Ð277. *Stable isotope geochemistry* **43**, (2001).

25. Behnke, M. I. *et al.* Aquatic biomass is a major source to particulate organic matter export in large Arctic rivers. *Proceedings of the National Academy of Sciences* **120**, e2209883120 (2023).

26. Wei, B. *et al.* Dispersal and aging of terrigenous organic matter in the Pearl River Estuary and the northern South China Sea Shelf. *Geochim. Cosmochim. Acta* **282**, 324–339 (2020).

27. Andersson, A. *et al.* Regionally-varying combustion sources of the January 2013 severe haze events over eastern China. *Environ. Sci. Technol.* **49**, 2038–2043 (2015).

28. Fritz, M. *et al.* Eastern Beringia and beyond: late Wisconsinan and Holocene landscape dynamics along the Yukon Coastal Plain, Canada. *Palaeogeogr. Palaeoclimatol. Palaeoecol.* **319**, 28–45 (2012).

29. Bouchard, T. J. *et al.* Brainstorming procedure, group size, and sex as determinants of the problem-solving effectiveness of groups and individuals. *Journal of Applied Psychology* **59**, 135 (1974).

30. Zazula, G. D. *et al.* New radiocarbon-dated vertebrate fossils from Herschel Island: implications for the palaeoenvironments and glacial chronology of the Beaufort Sea coastlands. *Arctic* 273–280 (2009).

31. Appleby, P. G. Chronostratigraphic techniques in recent sediments. *Tracking environmental change using lake sediments: basin analysis, coring, and chronological techniques* 171–203 (2001).

32. Hofmann, A. F. *et al.* Package 'AquaEnv'. (2016).

33. Zeebe, R. E. & Wolf-Gladrow, D. *CO2 in seawater: equilibrium, kinetics, isotopes*. (Gulf Professional Publishing, 2001).